Research Square

Preprints are preliminary reports that have not undergone peer review.
They should not be considered conclusive, used to inform clinical practice,
or referenced by the media as validated information.

A DIC-based surrogate model for assessing blunt ballistic trauma by deformable non-lethal kinetic projectiles

Huizhe Wang
Chinese People's Armed Police Force Engineering University
Zongmin Ma
Chinese People's Armed Police Force Engineering University
Nan Zhang
Chinese People's Armed Police Force Engineering University
Hongwei Zhuang
zhuanghw01@163.com

Chinese People's Armed Police Force Engineering University

Article

Keywords: non-lethal kinetic projectiles, digital image correlation, Surrogate model, thoracic injury assessment

Posted Date: February 26th, 2026

DOI: https://doi.org/10.21203/rs.3.rs-8708040/v1

License: This work is licensed under a Creative Commons Attribution 4.0 International License.
Read Full License

Additional Declarations: No competing interests reported.

A DIC-based surrogate model for assessing blunt ballistic trauma by deformable non-lethal kinetic projectiles

Huizhe Wang[1,2,a],Zongmin Ma[2,b],Nan Zhang[2,c],Hongwei Zhuang[2,d*]

[1]Graduate Brigade, Engineering University of PAP, Xi'an, China

[2]School of Equipment Management & Support, Engineering University of PAP, Xi'an, China

[a]email: 1925738085@qq.com, [b]email: 1046611314@qq.com, [c]email: 2544623588@qq.com, [d*]Corresponding Author: zhuanghw01@163.com

Abstract

Non-lethal kinetic projectiles (NLKP) are designed to incapacitate targets through pain compliance without causing fatal injuries. Traditional injury risk assessment for rigid NLKPs typically employs the projectile's displacement within the impact zone as a surrogate to estimate the compression displacement of the target organ. However, accurately quantifying the injury effects of deformable NLKPs remains challenging, as significant projectile deformation precludes precise measurement. Drawing upon Post-Mortem Human Subject (PMHS) literature data, this study constructs a surrogate model for thoracic injury risk assessment by conducting blunt impact tests on a Hybrid III 50th percentile male dummy. This model enables the prediction of AIS 2+ thoracic injury risk based on the projectile's physical parameters and measurable compression displacement. Applying this surrogate model to evaluate the 12-gauge bean bag round, results indicate that at a terminal velocity of 60m/s, the probability of inducing AIS 2+ thoracic injury is significantly below 50%.

Keyword: non-lethal kinetic projectiles; digital image correlation; Surrogate model; thoracic injury assessment

1 Introduction

Non-lethal kinetic projectiles, which are designed to incapacitate targets without causing fatal injuries, are widely used in law enforcement and stability operations. However, practical deployment and statistics indicate that excessive injury outcomes could still occur[1]. Impacts to vulnerable regions such as the thorax and abdomen may induce rib fractures, internal organ bleeding, and cardiopulmonary dysfunction[2-5]. Experimental studies of blunt ballistic trauma have established a mature evaluation framework by integrating sensor measurements with biomechanical dummies[6], animal models[7,8], post-mortem human subjects (PMHS)[9-11], and physical surrogates[12,13]. A major limitation of these methods is the assumption that the projectile's kinematic response can be directly recorded by external monitoring systems (such as high-speed cameras or laser displacement sensors) and used as a surrogate to estimate the compression displacement of the target organ and assess injury risk. However, for deformable NLKP, the total observed displacement at time t, denoted as

$d_{observerved}(t)$, can be divided into two parts:

$$d_{observerved}(t) = d_1(t) + d_2(t) \quad (1)$$

Where d_1 represents the compression displacement of the target organ, d_2 represents the longitudinal deformation displacement of the projectile .

The stiffness of rigid NLKP is substantially higher than that of human thoracic tissue[14]; therefore, it can be reasonably approximated as a rigid body. Consequently, during impact, $d_2 \approx 0$, and $d_{observed}$ is effectively equivalent to the target organ compression. Conversely, for deformable or frangible projectiles($d_2 \neq 0$), the projectile undergoes viscoelastic or plastic deformation during high-speed impact. This deformation cannot be directly measured by conventional methods and remains unobservant. If this deformation is ignored or the projectile is assumed to be rigid, chest compression will be significantly overestimated. This reduces the accuracy of chest injury-assessment criteria such as the Blunt Criterion (BC) [15]and the Viscous Criterion ($VC_{\max}$)[16,17] ,which depend on chest compression and compression velocity.

To obtain reliable biomechanical responses under the impact of NLKPs, several approaches, such as mechanical surrogates, finite element simulation etc., are employed. Mechanical surrogates equipped with internal sensors provide repeatable, quantitative impact data and serve as standard substitutes for biological subjects[12,18,19]. However, for low-mass projectiles, the most of energy dissipation is occurred at the initial impact process, which means that the original impact signals, transferring into the internal sensor, are hard to measure. Finite element simulation can effectively model the viscoelastic deformation of projectile[20-22]. Nevertheless, without adequate experimental calibration and validation, numerical predictions may deviate from real impact responses. Regarding optical methods, high-speed camera tracking of projectile-tail displacement is suitable for rigid impacts[8,9]. However, when subjected to deformable projectiles, if we neglect the longitudinal deformation displacement of the projectile, the injury risk of blunt impact on thorax will be potentially overestimating. Piezoelectric film micrometre-scale thickness enables it to be mounted conformally on curved targets and allows direct measurement of interfacial stress transfer[23], their application in high-speed impacts is often hindered by limited sampling bandwidth[24] and high system costs. Digital Image Correlation (DIC) tracks speckle markers to enable non-contact, full-field displacement/strain measurement. It is well-suited for high-speed transient deformation[25,26]. LeSueur[27] and Wen[28] validated DIC for blunt-impact measurements. For complex contact and large deformation, Wang[29] used 3D-DIC to reconstruct transient displacement fields under high-speed impact. Compared with conventional methods, 3D-DIC can still deliver non-contact, full-field displacement when contact sensors are constrained or when strong projectile-target coupling partially occludes the impact region. Validated against the NATO AEP-99 standard response corridors[30](Thorax injury risk assessment of non-lethal projectiles), this model is applied to quantitatively assess the injury risk of a 12-gauge bean bag projectile.

This study proposes a DIC-based surrogate injury assessment model to address the inability to directly quantify chest compression displacement in deformable NLKPs impacts. By quantifying the

dynamic displacement of speckles at the periphery of the impact zone, where the view is obstructed, we establish a mapping relationship to reconstruct the true central chest compression.This model has been validated against the NATO AEP-99[30] standard response corridors (thorax injury risk assessment of non-lethal projectiles) and is used to quantitatively assess the injury risk posed by 12-gauge bean bag projectile.

2 Material and Methods

This section outlines the test materials, the DIC system, the NLKP launcher, and the data-processing workflow. The experiments aim to build and validate a DIC-based surrogate model for damage assessment. All conditions followed relevant biomechanics standards to ensure repeatable and valid data.

2.1 Experimental subjects and instrumentation

2.1.1 Hybrid III 50th percentile male dummy

The Hybrid III 50th percentile male dummy, selected as the experimental surrogate to anthropometrically represent an average adult male, was characterized by a mass of 77.65 ± 1.18kg, a height of 1750 ± 10mm, and a chest depth of 221 ± 7.6mm, with the specific material properties of its critical tissues detailed in Table 1. Furthermore, to minimize environmental variance and its potential influence on the viscoelastic response of the skin and damping materials, the laboratory environment was strictly maintained at 23 ± 2℃ and 50 ± 5% relative humidity in accordance with 49 CFR Part 572[31] standards.

Table 1:Key parameters of the dummy tissues and organs

Tissue/Organ	Material / Grade	Material hardness	Material density
Skull	Steel A357	HBS20-35	2.7
Skin	Polyurethane resin	45-50(Shore A)	1.4
Skeleton	Steel 1018	HRC20-30	7.85
Lumbar spine	Rubber	—	—
Neck	Rubber	—	—

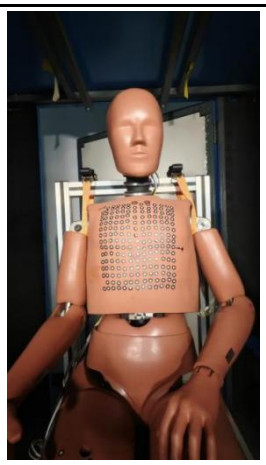


Figure 1: Hybrid III 50th percentile male dummy

2.1.2 Projectile types

Two types of NLKPs were used in this experiment, whose material properties are listed in Table 2.

(1) L5 plastic baton round, which has been made of polyurethane, is a cylindrical shape with mass 30g and 140g. Its complete PMHS blunt-impact test data has been available[11].

(2) A 12-gauge bean bag round, which consists of lead pellets enclosed in a nylon fabric bag and has a nominal caliber of approximately 18.5 mm with a total mass of 32 g, was selected to represent deformable NLKPs. To reduce variability, parameters of projectiles, such as mass, length and diameter, should be checked before launching, projectiles with relative errors (Eq. 2) exceeding 3% must be excluded.

Table 2: Material characteristics of the projectiles

Type	Mass (g)	Length (mm)	Diameter (mm)	Hardness (HD)
L5@140g	140	87.5	37	78
L5@30g	30	21.5	37	78
12-gauge bean bag round	40	—	18.5	—



Figure 2a: L5 baton round



Figure 2b: 12-gauge bean bag round

$$\delta_L = \frac{L_i - L_0}{L_0} \times 100\%, \quad \delta_m = \frac{m_i - m_0}{m_0} \times 100\% \tag{2}$$

Where L_i and L_0 represent the measured and standard length of projectiles, m_i and m_0 represent the measured and standard mass of projectiles.

The NLKP launching system, comprising a power supply, trigger unit, discharge unit is designed to deliver an adjustable launch velocity exceeding 10m/s while maintaining a repeatability $\leq \pm 3\%$. These performance metrics have been verified by an independent third-party laboratory(Test Report No. C25AA2501040067). To strictly verify the kinetic parameters during the impact experiments, the instantaneous projectile velocity was acquired using a dual-beam laser velocimeter aligned 10cm from the muzzle.

2.1.3 Digital Image Correlation

The DIC system was configured with a stereovision setup comprising two high-speed cameras

and dual flicker-free illumination sources, utilizing specialized speckle markers provided by XTDIC to track surface deformation. System calibration was executed using the Phantom Camera Control Application (PCC), while the subsequent post-processing and extraction of raw displacement-time curves were conducted using the XTDIC DSE3D strain analysis software. Detailed technical specifications for both the hardware components and the software suite are summarized in Tables 3 and 4.

Table 3: Hardware system

Equipment	Quantity	Specifications and Performance
High-speed cameras	2	Two Vision Research Inc. Phantom T3610 ultra-high-speed cameras with a Nikon 80–200 mm zoom lens; full-frame resolution and frame rate≥640×480 with 40,000 fps.
Dual flicker-free illumination sources	2	200 W flicker-free lights supplied by Xi'an York Technology Co., Ltd.
Speckle markers	195dots/set	Inner diameter 10 mm; self-adhesive; matte surface finish.

Table 4: Technical specifications of the software system

Metric	Specifications and Performance
Strain measurement range	0.005%-2000%; 2D strain accuracy≤20μs; 3D strain accuracy≤50μs.
Displacement measurement accuracy	0.01mm
Computation functions	3D displacement; strain X, strain Y, strain XY; maximum and minimum principal strain; von Mises strain; Tresca strain; shear angle; etc.

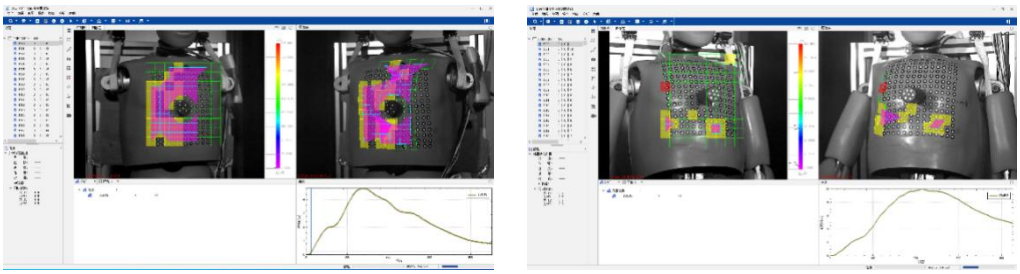


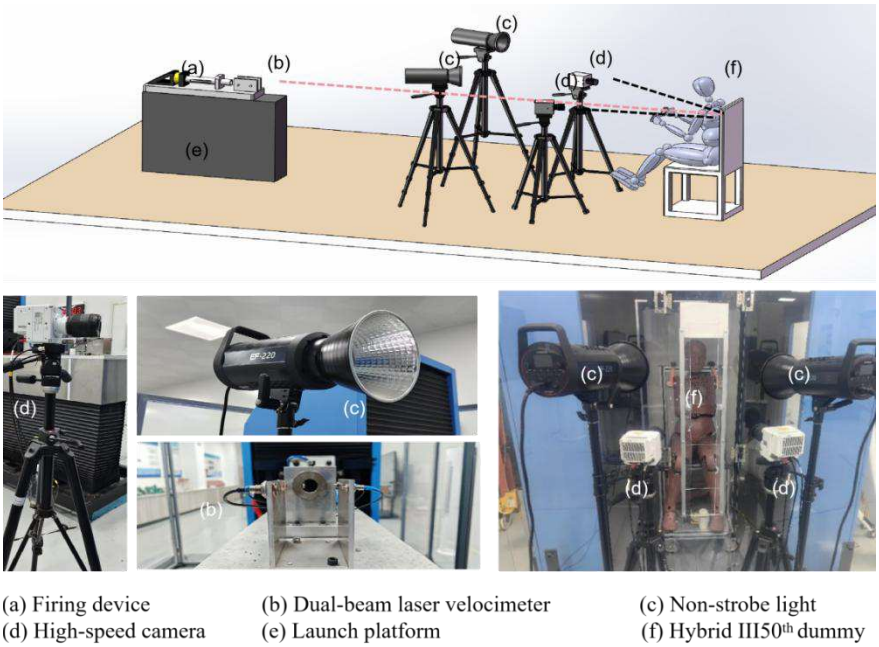
Figure 3: XTDIC DSE3D strain analysis software

2.2 Experimental setup

2.2.1 Instrument setup

As depicted in the experimental layout schematic (Figure 4), the dummy was positioned in a seated posture and firmly secured to a rigid test bench using high-strength restraint straps, thereby effectively constraining displacement in non-impact directions. The specific impact point was designated at the mid-sternum, spatially aligned vertically with the level of the eighth rib and

horizontally along the mid-sagittal line of the sternum.



(a) Firing device (b) Dual-beam laser velocimeter (c) Non-strobe light
(d) High-speed camera (e) Launch platform (f) Hybrid III50th dummy

Figure 4: Schematic diagram of experimental layout

To capture the transient impact response, two high-speed cameras were positioned bilaterally relative to the surrogate and focused on the designated impact center, forming an included angle of $\alpha = 30^{\circ}$ as illustrated in Figure 5. Data transmission was managed via a network switch to a host computer, while the triggering system was specifically engineered to mitigate intense electromagnetic interference generated by the launch platform. To ensure precise synchronization, a high-sensitivity acoustic sensor was employed in a master-trigger configuration; upon detecting the launch acoustic pulse, the signal was conditioned and converted into a TTL[32] output, which simultaneously triggered both cameras to align image acquisition with the projectile flight timeline.

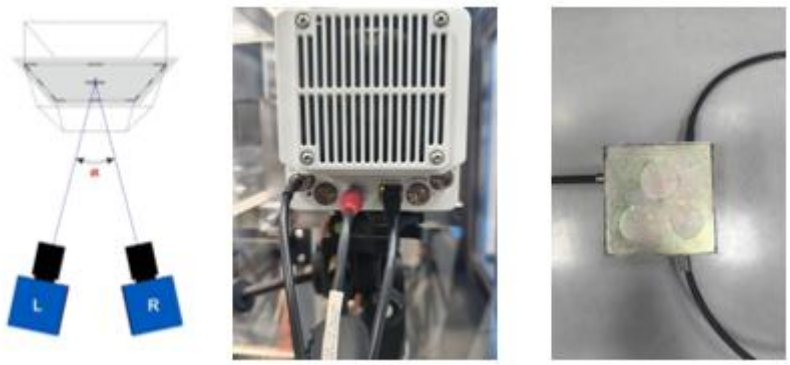


Figure 5: Layout diagram of high-speed camera

2.2.2 System calibration

To guarantee precise spatial reconstruction within the DIC framework, a high-precision ceramic calibration plate was employed,with specifications detailed in Table 5. The calibration process

involved positioning the plate 3 cm anterior to the dummy's impact center to acquire eighteen image sets across varying orientations, which were subsequently analyzed using the PCC software to achieve a residual score of ≤ 0.1 pixels. To preserve data integrity, the optical configuration was strictly maintained without adjustment following calibration, as illustrated in Figure 6,and any displacement of the cameras necessitated a complete recalibration sequence.

Table 5: Parameters of the ceramic calibration plate

	Area	Target array	Target daimeter	Center-to-center spacing
Parameter	400mm×300mm	15×11	7mm	23 mm

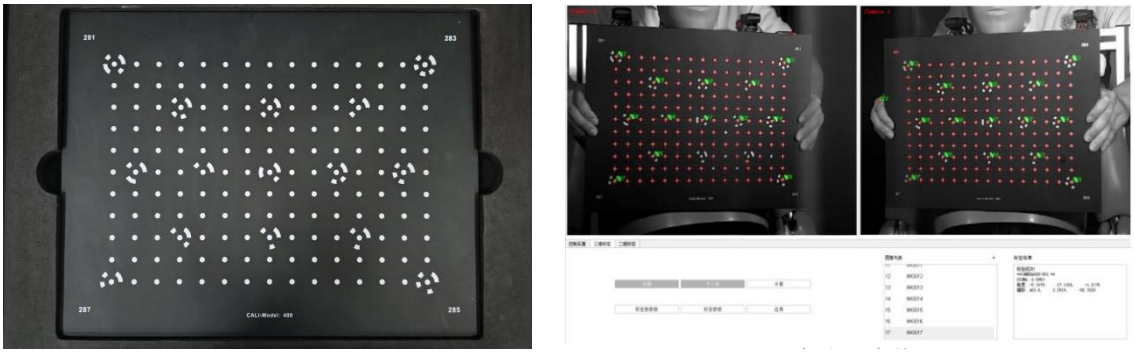


Figure 6: Calibration plate and calibration parameter settings

2.2.3 Test condition

To facilitate a direct biomechanical comparison, the dummy was subjected to blunt impacts under conditions identical to the PMHS datasets established by Bir[11] (Table 6), after which a rigorous inspection protocol was implemented to ensure that any skin rupture or component damage was repaired or replaced prior to subsequent testing. Furthermore, to guarantee statistical reliability, each experimental condition comprised $N = 10$ [33]valid trials. Consequently, any trial characterized by projectile tumbling or impact point deviation exceeding a radial threshold of $r > 1.5\text{cm}$ from the designated center was systematically discarded and repeated.

Table 6: PMHS: impact test conditions

Condition	Projectile type	Impact location	Velocity (m/s)
1	L5@140g	Chest	20
2	L5@140g	Chest	40
3	L5@30g	Chest	60

2.3 Data Processing

2.3.1 Data Processing and Scaling

Given that the raw displacement-time curves acquired by the DIC system were inevitably contaminated by high-frequency noise and mechanical jitter resulting from the high-velocity impact events, signal conditioning was requisite to isolate the underlying biomechanical response.

Consequently, the displacement data were filtered in strict accordance with SAE J211[34]and ISO 6487[35]standards utilizing a zero-phase, fourth-order Butterworth low-pass filter (Channel Frequency Class, CFC), the time-domain difference equation of which is expressed as:

$$Y(t) = a_0 X(t) + a_1 X(t-1) + a_2 X(t-2) + b_1 Y(t-1) + b_2 Y(t-2).$$

Where

$$\begin{cases} w_d = 2\pi \times \mathrm{CFC} \times 2.0775 \\ w_a = \sin(w_d \times T/2) / \cos(w_d \times T/2) \\ a_0 = w_a^2 / (1 + \sqrt{2} \times w_a + w_a^2) \\ a_1 = 2 \times a_0 \\ a_2 = a_0 \\ b_1 = -2 \times (w_a^2 - 1) / (1 + \sqrt{2} \times w_a + w_a^2) \\ b_2 = (-1 + \sqrt{2} \times w_a - w_a^2) / (1 + \sqrt{2} \times w_a + w_a^2) \end{cases} \tag{3}$$

Where $X(t)$ and $Y(t)$ denote the raw input signal and the filtered output, respectively, whereas T signifies the sampling interval and CFC corresponds to the 3dB cutoff frequency defined by the selected channel class.

Although Eq.(3) fundamentally describes a second-order recursive filter, a phaseless fourth-order response strictly compliant with the CFC 1000 specification of NATO AEP-99[30]was achieved by applying the filter bi-directionally to eliminate phase shift. Subsequently, to compensate for anthropometric discrepancies between the surrogate and the human subjects, and to facilitate a direct comparison with the PMHS datasets reported by Bir[11], the filtered displacement-time curves were normalized utilizing proportional scaling law[30]expressed as:

$$D_{norm}(t) = D_{filter}(t) \times \frac{D_{PMHS}}{D_{Dummy}} \tag{4}$$

Where $D_{norm}(t)$ represents the normalized dummy chest displacement-time data, $D_{filter}(t)$ denotes the filtered dummy displacement, D_{Dummy} refers to the standard chest depth of the Hybrid III 50th percentile dummy (221 mm), D_{PMHS} represents the reference chest depth of a 50th percentile adult male (236 mm).

Following this preprocessing phase, to mitigate experimental variability and establish a robust representative response, the arithmetic mean of the time-resolved displacement was computed across the ten valid trials ($N = 10$ [33]) for each impact condition, as mathematically defined by Eq. (5).

$$\bar{D}_j(t) = \frac{1}{10} \sum_{i=1}^{10} D_{ji}(t) \tag{5}$$

Subsequently, the chest compression velocity, denoted as $\overline{D}_j'(t)$, was derived via numerical

differentiation of the mean displacement signal utilizing the standard central difference algorithm prescribed by SAE J211, expressed in Eq. (6).

$$\bar{D}_j^{'}(t)=\frac{8\left(\bar{D}_j(t+\Delta t)-\bar{D}_j(t-\Delta t)\right)-\left(\bar{D}_j(t+2\Delta t)-\bar{D}_j(t-2\Delta t)\right)}{12\Delta t} \tag{6}$$

Finally, to quantify the soft-tissue injury risk, the Viscous Criterion (VC)—representing the instantaneous product of compression velocity and normalized compression ratio—was calculated, with the maximum value (VC_{max}) for each condition determined according to Eq. (7).

$$\mathrm{VC}_{\max}=\max\left(\frac{\bar{D}_j^{'}(t)\cdot\bar{D}_j(t)}{D_0}\right) \tag{7}$$

2.3.2 Validation Benchmark

To establish a rigorous validation benchmark for the three standard impact conditions outlined in Table 6, the biomechanical response corridors defined in the NATO AEP-99 standard were adopted as the reference ground truth. As delineated in Tables 7 and 8, these corridors quantify the admissible boundaries for the chest-center displacement and the maximum Viscous Criterion ($VC_{\max}$) under varying kinetic-energy loads. Consequently, the efficacy of the proposed surrogate injury-assessment model was evaluated by determining whether the reconstructed displacement trajectories and calculated injury criteria fell strictly within these biomechanical response corridors.

Table 7: Validation of PMHS chest displacement under impact from L5 plastic baton round

Test condition	Lower time bound (ms)	Lower displacement bound (mm)	Upper time bound (ms)	Upper displacement bound (mm)
1	0	0	0	0
	2	12	0.5	10
	5	18	2.3	20
	—	—	5	26
2	0	0	0	0
	2	20	1	40
	8	38	6	70
3	0	0	0	0
	1	5	0.5	12.5
3	8	12	8	38

Table 8: Boundary limits of chest $VC_{\max}$ for PMHS impacted by L5 plastic baton round

Test condition	$\mathrm{VC}_{\max}$ limits (m/s)
1	[0.24, 0.51]
2	[0.65, 2.35]
3	[0.14, 0.6]

2.3.3 Independent Variables of the Injury-Assessment Surrogate Model

To construct the multivariate injury-assessment surrogate model, the experimental dataset acquired from the controlled surrogate impact tests was utilized to define a set of candidate independent variables representing the kinematic and geometric characteristics of the collision. Specifically, the potential predictors evaluated included projectile mass, impact velocity, kinetic energy, momentum, specific kinetic energy, and the radial distance from the tracking speckle to the impact center, the full definitions and units of which are systematically itemized in Table 9.

Table 9: Fitting independent variables and dependent variable

Independent variables								**Dependent variable**
m	v	E	P	PE	C_0	PC_0	dis	K

3 Results

Following the exclusion of trials characterized by clear outliers or abnormal impact attitudes, 150 valid L5 samples has been retained for the development and validation of the surrogate model. Additionally, five valid 12-gauge bean bag rounds were selected for model application.

3.1 Feature analysis of speckle-displacement signals

Upon examining the raw kinematic data acquired by the XTDIC system, the displacement-time curves recorded at the periphery of the impact zone exhibited a distinct morphological consistency with the standard biomechanical response corridors derived from PMHS data, despite a marked reduction in signal magnitude. As exemplified by the representative response curve for Condition 2 (Figure 7), while the peak peripheral displacement was significantly attenuated to approximately 5.1 mm-a value substantially lower than the typical central chest deflection range (30-50 mm)-the temporal phase characteristics remained highly synchronized with the external ballistic loading event. Specifically, the temporal milestones, including the initiation of the rapid loading phase at $t = 0$ ms and the attainment of peak displacement at approximately $t = 5.5$ ms, exhibited a waveform topology parallel to the AEP-99[30] validation corridors. These signal characteristics indicate that, although the stress-wave dissipation inherent to the viscoelastic skin and soft tissues results in amplitude attenuation, the linear kinematic transfer function between the peripheral surface response and the concealed central compression is effectively preserved during the loading and unloading-rebound phases.

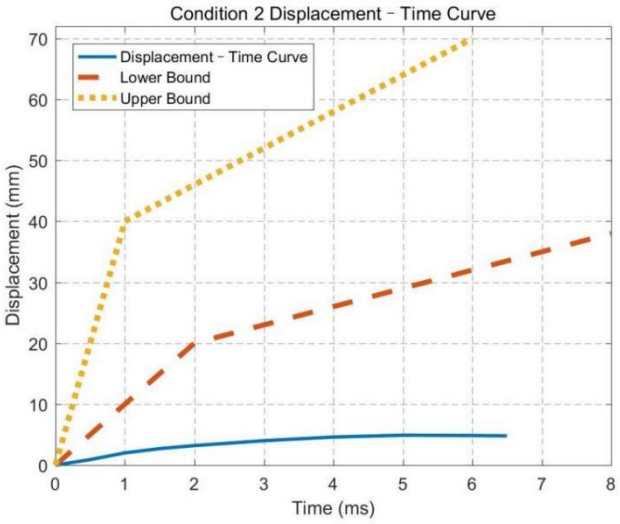


Figure 7: Condition 2 ($dis = 11.55\text{cm}$): original displacement–time curve

Predicated on this observation of linear topological similarity, an equivalent-displacement mapping hypothesis was formulated to reconstruct the true central compression from the peripheral measurements, mathematically expressed as:

$$D_{\text{eq}}(t) = K \cdot D_{norm}(t) \tag{8}$$

Where $D_{\text{eq}}(t)$ represents the true central compression displacement, $D_{norm}(t)$ denotes the peripheral speckle displacement, K serves as the scaling factor.

To quantify this scaling factor, a functional relationship was established based on the dataset of 150 valid trials. Subsequently, multivariate linear regression was employed to correlate the candidate independent variables with the empirically derived K values, thereby formally constructing the surrogate injury-assessment surrogate model for NLKPs.

3.2 Surrogate model development and validity verification

Given that kinematic parameters such as kinetic energy (E) and momentum (P) are mathematically derived from projectile mass (m) and velocity (v), the initial dataset inevitably contained intrinsic dependencies. To mitigate the risk of parameter instability and overfitting caused by such multicollinearity[30], a Variance Inflation Factor (VIF) analysis was conducted on the candidate predictors (Table 10). The analysis revealed that the VIF values for derived variables-specifically kinetic energy, momentum, and specific kinetic energy-approached infinity or significantly exceeded the standard threshold of 10, indicating severe information redundancy. Consequently, these highly collinear variables were excluded from the regression model, while v , PC_0 , dis were retained as the core independent variables.

Table 10: VIF test for independent variables

Independent variables	C_0	PE	E	m	P

VIF	119700	Inf	Inf	12563.97	770.5

To verify that the screened variable set satisfied the independence assumption required for multivariate linear regression, a Pearson correlation analysis was performed (Figure 8). The resulting correlation heatmap demonstrates that the absolute correlation coefficients between the retained predictors remained below 0.42, confirming that the selected feature set effectively minimizes redundant information while adhering to the orthogonality requirements of the regression framework.

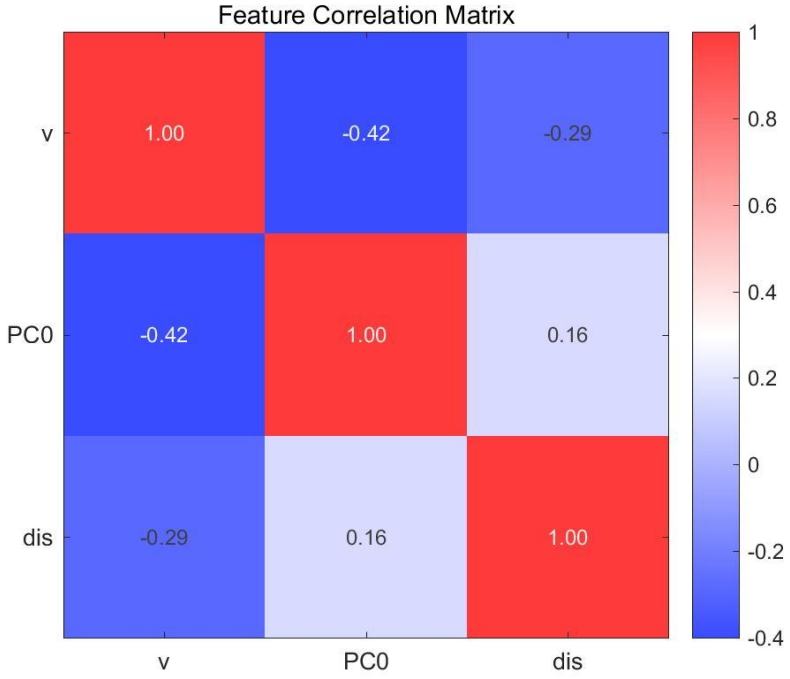


Figure 8: Heatmap of predictor correlations

Furthermore, a Principal Component Analysis (PCA) was employed to ascertain whether the three retained predictors (v, PC_0, dis) constitute an irreducible feature set (Figure 9). The analysis of cumulative explained variance indicated that the first two principal components (PC1 and PC2) accounted for only 81.5% of the total variance, falling short of the generally accepted 95% information retention criterion. Full information recovery (100% variance) was achieved only upon the inclusion of the third component, providing robust statistical evidence that all three predictors offer unique and indispensable contributions to the feature space.

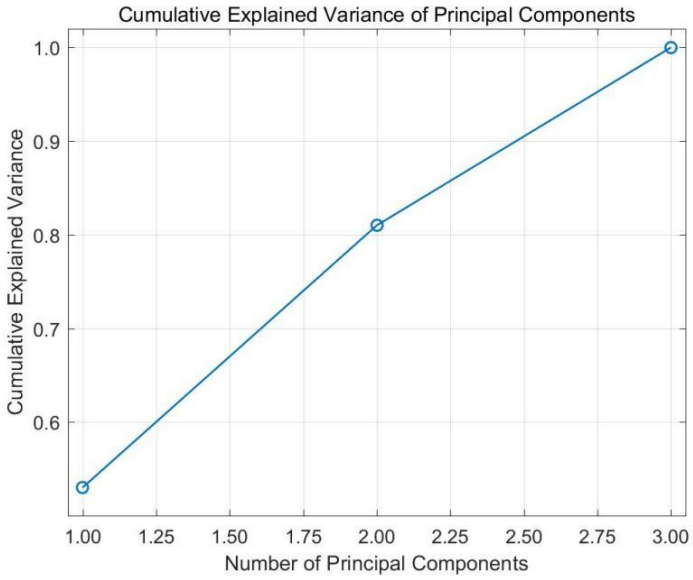


Figure 9: Cumulative explained variance of principal components

Based on these feature selection results, a multivariate linear regression model was constructed to predict the displacement scaling factor (K). The final model, expressed in Eq. (9), achieved a coefficient of determination $R^2 = 0.68$. Considering the inherent nonlinearity and stochastic variability associated with the viscoelastic response of the biomechanical surrogate (dummy skin and damping materials), this goodness-of-fit indicates that the model successfully captures the primary mapping relationship between the peripheral kinematic observables and the central compression scaling factor.

$$\hat{K} = -0.19 - 0.035v + 0.0165PC_0 + 0.7715dis \tag{9}$$

Incorporating this scaling factor into the Viscous Criterion framework defined by NATO AEP-99, the generalized injury-assessment equation for deformable NLKPs is derived as:

$$\begin{aligned} \mathrm{VC}_{\max} &= \frac{(\hat{K}D_{dis}) \cdot (\hat{K}D'_{dis})}{D_0} \\ &= \frac{(-0.19 - 0.035v + 0.0083m^2v^3 / S + 0.77dis)^2 D_{dis} \cdot D'_{dis}}{223} \end{aligned} \tag{10}$$

3.3 Biomechanical validation of the surrogate model

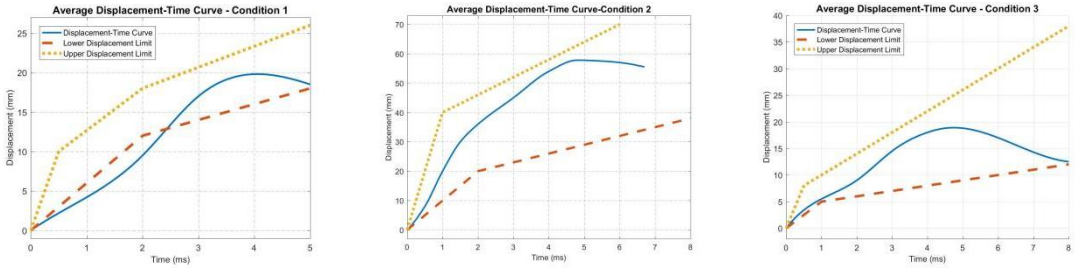
To rigorously evaluate the predictive fidelity and robustness of the developed surrogate model across a spectrum of impact severities, three representative test cases (Conditions 1-3) were stochastically selected from the valid dataset of 150 trials. For each validation case, the specific kinematic inputs, comprising v, PC_0, dis were extracted and listed in Table 11. By substituting these experimentally acquired parameters into the derived multivariate regression equation (Eq. 9) and the reconstruction function (Eq. 10), the corresponding displacement scaling factors (K) were computed as 6.67, 8.17, and 4.34 for Conditions 1, 2, and 3, respectively.

Table 11: Selected condition

Condition	v	PC_0	dis	$\hat{K}$
Condition 1	19.88	7.21	9.64	6.67
Condition 2	39.5	50.05	11.55	8.174
Condition 3	59.52	8.99	8.36	4.34

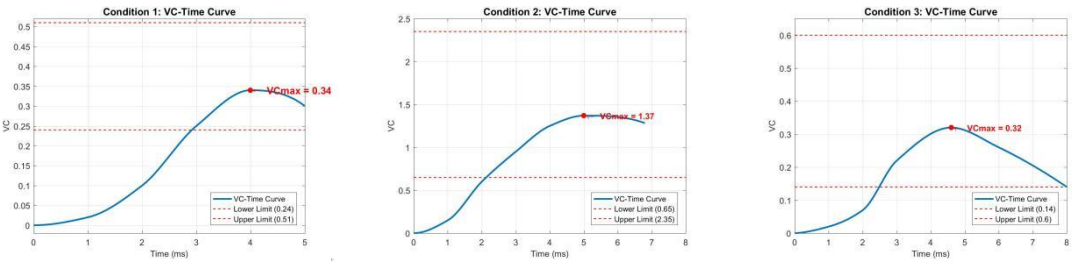
Subsequently, the time-resolved central chest compression was reconstructed and compared against the standard biomechanical response corridors defined in NATO AEP-99, as illustrated in Figure 10. The results demonstrate a high degree of morphological concordance between the predicted trajectories and the PMHS reference corridors; specifically, the reconstructed curves not only strictly confine their peak magnitudes within the admissible validation boundaries but also accurately replicate the characteristic waveform topologies, including the rapid loading rate during the initial compression phase, the temporal synchronization of the peak displacement, and the nonlinear recovery trends observed during the unloading-rebound phase.

Further quantitative assessment of the injury risk was conducted via the Viscous Criterion (VC) time histories presented in Figure 11. The analysis confirms that the calculated maximum VC values for all validation conditions (Condition 1: 0.34m/s; Condition 2: 1.37m/s; Condition 3: 0.32m/s) fall strictly within the requisite biomechanical boundary limits (e.g., the calculated $VC_{\max}$ of 1.37m/s for Condition 2 lies well within the [0.65, 2.35]m/s corridor). These validation results provide robust statistical evidence that the proposed DIC-based surrogate model effectively overcomes the occlusion challenges inherent in blunt-impact testing, enabling the accurate reconstruction of rigid projectile impact responses and ensuring reliable biomechanical assessments consistent with international standards.



Condition 1: 6.67× amplification factor | Condition 2: 8.17× amplification factor | Condition 3: 4.4× amplification factor

Figure 10. Displacement-time curves for conditions 1-3 after scaling-factor amplification



Condition 1: 6.67× | Condition 2: 8.17× | Condition 3: 4.4×

amplification factor amplification factor amplification factor

Figure 11. VC-time curves for conditions 1-3 after scaling-factor amplification

3.4 Injury-effect assessment of the 12-gauge bean bag round

To empirically verify the generalization capability of the proposed surrogate model in assessing blunt trauma from deformable NLKPs, a 12-gauge bean bag round was tested under impact conditions kinematically comparable to the L5 rigid projectile trials. Table 12 summarizes the physical parameters measured synchronously by the DIC and velocimetry systems. Substituting these parameters into Eq. (9) yields the optimal displacement scaling factor $\hat{K} = 5.39$.

Table 12: Measured physical parameters

m	***v***	***PC*$_0$**	***dis***	$\hat{K}$
31.85	60.26	9.98	9.74	5.39

Applying this predicted scaling factor to the raw peripheral displacement data, the true central chest compression history and the corresponding Viscous Criterion (VC) evolution were reconstructed, as presented in Figure 12. The reconstructed displacement-time curve (Figure 12a) exhibits a smooth, nonlinear loading trajectory culminating in a peak compression of approximately 10.2 mm; notably, in contrast to the sharp recoil observed in rigid projectile impacts at equivalent energy levels, the deformable bean bag round displays a significantly more gradual unloading phase. This distinct hysteresis behavior indicates that the viscoelastic deformation of the projectile filling, coupled with structural compliance, effectively prolongs the projectile-target contact duration and dissipates impact energy through internal viscous damping rather than pure elastic rebound.

The quantitative injury risk assessment, derived from the reconstructed kinematics (Figure 12b), yielded a maximum $VC_{max} = 0.10\,m/s$. According to the injury risk functions defined in the NATO AEP-99 standard, this value is statistically far below the 50% probability threshold for AIS2+ (moderate or severe) thoracic injury and remains well within the safe operational limit of 0.8m/s, thereby indicating a low injury risk.

A comparative analysis of equivalent energy conditions further elucidates the safety mechanism of deformable NLKPs. Although the 12-gauge bean bag round has a comparable kinetic energy level to the high-velocity L5 rigid projectile (Condition 3), its induced biomechanical response is considerably milder. It is only comparable to a 30g rigid baton round impacting at a much lower velocity of approximately 45m/s. This down-scaling effect demonstrates how the viscoelastic nature of the projectile absorbs kinetic energy and reduces peak loading rates, confirming the "high energy availability, low injury potential" design philosophy of deformable NLKPs.

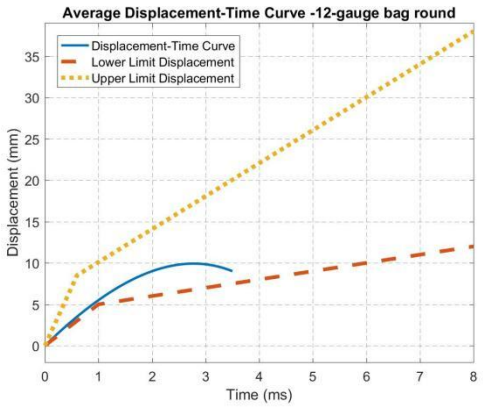


Figure 12a: Equivalent displacement-time curve of the 12-gauge bean bag round

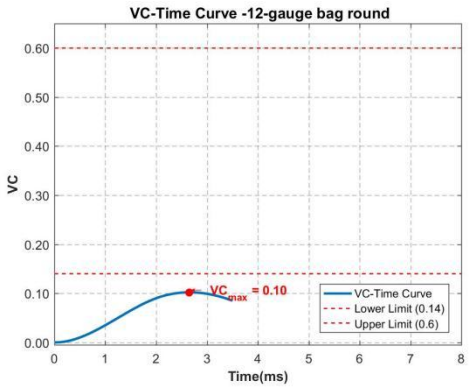


Figure 12b: Equivalent VC-time curve of the 12-gauge bag round

4 Discussion

The proposed non-contact injury-assessment surrogate model has been shown to have distinct advantages, the most significant of which is the utilisation of the DIC system. This system is capable of fundamentally addressing the instrumentation limitations encountered in conventional ballistic testing. In contrast to previous methodologies that relied on embedded physical sensors, such as the strain gauges and piezoelectric sensors employed by Dancerel-Bourlon[36]. to capture local signals, the full-field optical measurement approach adopted in this study resolves the critical issue regarding the inability to directly measure the central chest compression displacement within the projectile-target impact zone. Specifically, this method overcomes the inherent constraints where the large-scale deformation of NLKPs couples with the target surface to obscure the contact interface, rendering the peak compression of the thorax physically unobservable by traditional high-speed imaging or laser displacement sensors.

From a statistical perspective, the reliability of the model was subjected to rigorous scrutiny through the implementation of a VIF analysis, a process that enabled the elimination of highly collinear derived variables. Subsequent to this, a PCA was employed to ascertain that the three retained core predictors (v, PC_0, dis) accounted for 100% of the variance in the original feature space. This analysis facilitated the construction of a robust multivariate linear regression model. Although the coefficient of determination (R^2) approximated 0.7, it is noteworthy that this value is statistically significant given the intrinsic nonlinear viscoelastic response and the material heterogeneity associated with the experimental surrogate. This observation serves as an indication that the model successfully encapsulates the primary mapping relationship between the peripheral kinematic inputs and the central displacement scaling factor (K).

In the three validation trials involving the rigid L5 projectile (Conditions 1-3), the reconstructed equivalent displacement-time curves demonstrated a consistent alignment with the NATO AEP-99[30] acceptance corridors, particularly at the points of peak deflection. Furthermore, the predicted values

for the $VC_{\max}$ remained strictly within the requisite biomechanical boundary limits. For instance, the Condition 1 prediction of 0.34 m/s falls well within the 0.24-0.51m/s interval. This provides robust evidence that this statistical surrogate model accurately captures the energy-transfer mechanics characterizing blunt ballistic impacts.

The application of the model to the 12-gauge bean bag round further elucidated a distinct energy-dissipation mechanism specific to deformable projectiles. Despite the 12-gauge bean bag round possessing kinetic energy at 60m/s comparable to that of the high-risk 30g L5 rigid projectile (Condition 3), the induced VC_{max} was restricted to merely 0.10m/s, a value substantially below the safety threshold of 0.8 m/s defined by the NATO AEP-99 standard. This implies a minimal probability of sustaining AIS 2+ (Abbreviated Injury Scale) thoracic injuries, such as rib fractures or organ contusion. The underlying safety mechanism is attributed to the viscoelastic nature and structural behavior of the projectile: upon impact, the bean bag undergoes significant macroscopic flattening while exhibiting viscoelastic damping characteristics. Consequently, the mitigation of injury risk is not merely a function of energy dissipation but also a result of the redistribution of impulse over a larger effective contact area, which reduces localized stress concentrations on the thoracic cage. This process also prolongs the projectile-target interaction duration, "smoothing" the impact load and significantly reducing the efficiency with which kinetic energy is converted into potentially injurious biomechanical responses.

Notwithstanding the demonstrated predictive performance, it must be acknowledged that the scaling factor K was calibrated primarily using the rigid L5 dataset, which may introduce generalization errors when applied directly to deformable NLKPs with varying material properties. However, given the substantial safety margin observed between the measured VC_{max} and the injury threshold (0.8m/s), the conclusion regarding the low lethality of the tested rounds remains robust even when accounting for potential model uncertainties. Future research will focus on two distinct avenues to enhance model applicability: first, the integration of high-fidelity human finite-element models will facilitate the augmentation of experimental data with simulated internal stress-field measurements[20], thereby supporting the precise calibration of surrogate-model coefficients for deformable projectiles; second, the expansion of the experimental database to encompass impacts across diverse angles and anatomical locations will be instrumental in refining the model's validity under complex, real-world operational conditions.

5 Conclusions

Deformable less-lethal kinetic projectiles undergo large, nonlinear deformation. This makes chest-compression response hard to measure directly. We developed a DIC-based, full-field, non-contact injury-assessment surrogate model. The model maps peripheral speckle displacement to central compression. It mitigates measurement occlusion and interference. L5 rigid-projectile tests confirmed its statistical reliability and biomechanical validity consistent with AEP-99. Tests on a 12-gauge bean bag round showed a low peak viscous response at 60m/s, $VC_{\max} = 0.10\text{m/s}$, well below

the injury threshold. This quantifies a “high energy-low injury” dissipation mechanism driven by structural deformation. The model may still have some generalization error. Even so, it offers a new path for blunt-impact injury risk assessment of deformable, less-lethal kinetic projectiles.

6 Acknowledgement

The authors would like to thank the anonymous reviewers and the editor for their constructive comments and suggestions that improved the quality of this manuscript. We also appreciate the support provided by the School of Equipment Management & Support, Engineering University of PAP during the experimental phase.

7 Authors’ contributions

Huizhe Wang: Conceptualization, Methodology, Software, Investigation, Formal analysis, Writing-original draft, Visualization. Zongmin Ma: Data processing, Validation, Software, Formal analysis. Nan Zhang: Investigation, Resources, Writing-review & editing. Hongwei Zhuang: Conceptualization, Supervision, Project administration, Writing - review & editing.

8 Competing interests

The author(s) declare no competing interests.

9 Data availability statement

The datasets generated during the current study, including the raw DIC displacement data and impact response curves, are available from the corresponding author on reasonable request. The biological response data (Post-Mortem Human Subjects) used for validation were obtained from previously published studies[11] and the NATO AEP-99 standard[30].

10 Funding

This study was supported by funding projects with grant numbers 2019-JCJQ-ZD-115-00 and MKY202324.

References

[1]Ifantides, C. *et al.* Ophthalmic injuries by less-lethal kinetic weapons during the US George Floyd protests in Spring 2020. *JAMA ophthalmology* **139**, 242-244. https://doi.org/10.1001/jamaophthalmol.2020.5325 (2021).

[2]Guenther, T. M., Gustafson, J. D., Wozniak, C. J., Zakaluzny, S. A. & Utter, G. H. Penetrating thoracic injury from a bean bag round complicated by development of post-operative empyema. *Journal of surgical case reports* **2020**, rjaa078. https://doi.org/10.1093/jscr/rjaa078 (2020).

[3]Olson, K. A. *et al.* Penetrating injuries from “less lethal” beanbag munitions. *New England journal of medicine* **383**, 1081-1083. https://doi.org/10.1056/nejmc2025923 (2020).

[4]Rezende-Neto, J. *et al.* Penetrating injury to the chest by an attenuated energy projectile: a case report and literature review of thoracic injuries caused by" less-lethal" munitions. *World Journal of Emergency Surgery* **4**, 26. https://doi.org/10.1186/1749-7922-4-26 (2009).

[5]Schalet, G., Davis, B., Gomez, M., Dickhudt, T. & Puente, I. Acute cardiac tamponade secondary to nonpenetrating injury from gunshot with beanbag round: A case report and literature review. *Trauma Case Reports* **42**, 100733. https://doi.org/10.1016/j.tcr.2022.100733 (2022).

[6]Kapeles, J. A. & Bir, C. A. Human effects assessment of 40-mm nonlethal impact munitions. *Human Factors and Mechanical Engineering for Defense and Safety* **3**, 2. https://doi.org/10.1007/s41314-019-0017-5 (2019).

[7]Langlet, A., Pavier, J., Eches, N. & Bailly, P. Study of less lethal projectiles blunt impacts on the thorax by experiments on pig thoracic cages and numerical simulations. *Computer Methods in Biomechanics and Biomedical Engineering* **18**, 1970-1971. https://doi.org/10.1080/10255842.2015.1069583 (2015).

[8]Pavier, J. *et al.* Experimental study of the coupling parameters influencing the terminal effects of thoracic blunt ballistic impacts. *Forensic Science International* **252**, 39-51. https://doi.org/10.1016/j.forsciint.2015.04.004 (2015).

[9]Bir, C., Viano, D. & King, A. Development of biomechanical response corridors of the thorax to blunt ballistic impacts. *Journal of biomechanics* **37**, 73-79. https://doi.org/10.1016/s0021-9290(03)00238-0 (2004).

[10]Bir, C. & Viano, D. C. Design and Injury Assessment Criteria for Blunt Ballistic Impacts. *Journal of Trauma and Acute Care Surgery* **57**, 1218-1224. https://doi.org/10.1097/01.ta.0000114066.77967.de (2004).

[11]Bir, C. A. *The evaluation of blunt ballistic impacts of the thorax*.https://www.proquest.com/openview/e1044a1b9c93bd66c533bde53db5991d/1?pq-origsite=gscholar&cbl=18750&diss=y(Wayne State University, 2000).

[12]Bracq, A. *et al.* On the use of a SEBS polymer gel block as a new ballistic target to assess blunt ballistic impacts: Application to a wide range of LLKE projectiles. *International Journal of Impact Engineering* **153**, 103874. https://doi.org/10.1016/j.ijimpeng.2021.103874 (2021).

[13]Bracq, A. *et al.* Rib fractures prediction method for kinetic energy projectile impact: from blunt ballistic experiments on SEBS gel to impact modeling on a human torso FE

model. *Forensic science international* **297**, 177-183. https://doi.org/10.1016/j.forsciint.2019.02.007 (2019).
[14]Kroell, C. K., Schneider, D. C. & Nahum, A. M. Impact tolerance and response of the human thorax II. *SAE Transactions*, 3724-3762. https://doi.org/10.4271/741187 (1974).
[15]Pavier, J., Langlet, A., Eches, N. & Jacquet, J.-F. On ballistic parameters of less lethal projectiles influencing the severity of thoracic blunt impacts. *Computer Methods in Biomechanics and Biomedical Engineering* **18**, 192-200. https://doi.org/10.1080/10255842.2013.789101 (2015).
[16]Robbe, C., Nsiampa, N., Papy, A. & Oukara, A. in *27th International Symposium on Ballistics.* 22-26.
[17]Sturdivan, L. M., Viano, D. C. & Champion, H. R. Analysis of injury criteria to assess chest and abdominal injury risks in blunt and ballistic impacts. *Journal of Trauma and Acute Care Surgery* **56**, 651-663. https://doi.org/10.1097/01.ta.0000074108.36517.d4 (2004).
[18]Chaufer, M. *et al.* in *Society for Experimental Mechanics Annual Conference and Exposition.* 121-128 (Springer).
[19]Qi, W., Zhuang, H. & Zhao, F. in *International Conference on P2P, Parallel, Grid, Cloud and Internet Computing.* 543-553 (Springer).
[20]Bracq, A. *et al.* Numerical recreation of field cases on a biofidelic human FE model involving deformable less-lethal projectiles. *Human Factors and Mechanical Engineering for Defense and Safety* **3**, 5. https://doi.org/10.1007/s41314-019-0022-8 (2019).
[21]Chen, C., Zhao, F. & Ma, Z. Numerical analysis of thorax injury caused by the blunt impact of SIR-X sponge grenade. *Human Factors and Mechanical Engineering for Defense and Safety* **7**, 2. https://doi.org/10.21203/rs.3.rs-2572503/v1 (2023).
[22]Nsiampa, N., Robbe, C. & Papy, A. Non-lethal projectile characterisation method: application to 40-mm SIR-X and condor NT901 projectiles. *Human Factors and Mechanical Engineering for Defense and Safety* **2**, 7. https://doi.org/10.1007/s41314-018-0014-0 (2018).
[23]Kalimuldina, G. *et al.* A Review of Piezoelectric PVDF Film by Electrospinning and Its Applications. *Sensors* **20**, 5214. https://doi.org/10.3390/s20185214 (2020).
[24]Min, H., Zhang, J. & Fan, M. Size effect of a piezoelectric patch on a rectangular plate with the neural network model. *Materials* **14**, 3240. https://doi.org/10.3390/ma14123240 (2021).
[25]Liu, B. *et al.* Digital image correlation in extreme conditions. *Thin-Walled Structures* **205**, 112589. https://doi.org/10.1016/j.tws.2024.112589 (2024).
[26]Sutton, M. A., Orteu, J. J. & Schreier, H. *Image correlation for shape, motion and deformation measurements: basic concepts, theory and applications*. (Springer Science & Business Media, 2009).
[27]LeSueur, J., Koser, J., Yoganandan, N. & Pintar, F. A. Three-Dimensional-Digital Image Correlation Methodology for Kinematic Measurements of Non-Penetrating Blunt Impacts. *Journal of Biomechanical Engineering* **146**, 114501. https://doi.org/10.1115/1.4065734 (2024).

[28]Wen, Y. *et al.* Test and Evaluation of Ballistic Helmet Performance Based on 3D-DIC Technology. *Transactions of Beijing institute of Technology* **42**, 463-470. https://doi.org/10.15918/j.tbit1001-0645.2021.104 (2022).
[29]Wang, H. *et al.* Dynamic response of ballistic plate based on mirror image 3D-DIC technique. *Mechanics of Time-Dependent Materials* **29**, 65. https://doi.org/10.1007/s11043-025-09806-8 (2025).
[30]Nato. STANREC 4744 edition 5 - aep 99 ed: b ver 1 Thorax injury risk assessment of non-lethal projectiles.https://nso.nato.int/nso/nsdd/main/standards?search=AEP-99 (NATO, 2021).
[31]Anthropomorphic Test Devices. *Code of Federal Regulations, Title 49, Part 572* (2025).
[32]Malik, S. A., Wang, L., Curtis, P. T. & Fernando, G. F. Self-sensing composites: In-situ detection of fibre fracture. *Sensors* **16**, 615. https://doi.org/10.3390/s16050615 (2016).
[33]Forrester, S. E. Selecting the number of trials in experimental biomechanics studies. *International Biomechanics* **2**, 62-72. https://doi.org/10.1080/23335432.2015.1049296 (2015).
[34]International, S. A. E. Instrumentation for Impact Test - Part 1 - Electronic Instrumentation. https://doi.org/10.4271/j211/1_201403 (2014).
[35]International Organization for, S. Road vehicles — Measurement techniques in impact tests — Instrumentation. https://doi.org/10.3403/30165195 (2015).
[36]Dancerel-Bourlon, E. *et al.* Experimental and numerical replication of blunt ballistic impact on a male thorax surrogate: study of rib fractures and lung injuries predictions. *Frontiers in Bioengineering and Biotechnology* **13**, 1704069. https://doi.org/10.3389/fbioe.2025.1704069 (2025).